Properties of Daily Helium Fluxes

M. Aguilar,[29] L. Ali Cavasonza,[1] G. Ambrosi,[36] L. Arruda,[27] N. Attig,[24] F. Barao,[27] L. Barrin,[15] A. Bartoloni,[42] S. Başeğmez-du Pree,[18,*] R. Battiston,[39,40] M. Behlmann,[10] J. Berdugo,[29] B. Bertucci,[36,37] V. Bindi,[20] K. Bollweg,[21] B. Borgia,[42,43] M. J. Boschini,[31] M. Bourquin,[16] E. F. Bueno,[18] J. Burger,[10] W. J. Burger,[39] S. Burmeister,[25] X. D. Cai,[10] M. Capell,[10] J. Casaus,[29] G. Castellini,[14] F. Cervelli,[38] Y. H. Chang,[47] G. M. Chen,[6,7] G. R. Chen,[23] H. S. Chen,[6,7] Y. Chen,[16,23] L. Cheng,[23] H. Y. Chou,[47] S. Chouridou,[1] V. Choutko,[10] C. H. Chung,[1] C. Clark,[10,21] G. Coignet,[3] C. Consolandi,[20] A. Contin,[8,9] C. Corti,[20] Z. Cui,[22,23] K. Dadzie,[10] A. Dass,[39,40] C. Delgado,[29] S. Della Torre,[31] M. B. Demirköz,[2] L. Derome,[17] S. Di Falco,[38] V. Di Felice,[44,†] C. Díaz,[29] F. Dimiccoli,[39] P. von Doetinchem,[20] F. Dong,[34] F. Donnini,[44,†] M. Duranti,[36] A. Egorov,[10] A. Eline,[10] J. Feng,[10] E. Fiandrini,[36,37] P. Fisher,[10] V. Formato,[44,†] C. Freeman,[20] C. Gámez,[29] R. J. García-López,[26] C. Gargiulo,[15] H. Gast,[1] M. Gervasi,[31,32] F. Giovacchini,[29] D. M. Gómez-Coral,[20] J. Gong,[34] C. Goy,[3] V. Grabski,[30] D. Grandi,[31,32] M. Graziani,[36,37] S. Haino,[47] K. C. Han,[28] R. K. Hashmani,[2] Z. H. He,[19] B. Heber,[25] T. H. Hsieh,[10] J. Y. Hu,[6,7] M. Incagli,[38] W. Y. Jang,[13] Yi Jia,[10] H. Jinchi,[28] G. Karagöz,[2] B. Khiali,[44,†] G. N. Kim,[13] Th. Kirn,[1] M. Konyushikhin,[10] O. Kounina,[10] A. Kounine,[10] V. Koutsenko,[10] D. Krasnopevtsev,[10] A. Kuhlman,[20] A. Kulemzin,[10] G. La Vacca,[31,32] E. Laudi,[15] G. Laurenti,[8] I. Lazzizzera,[39,40] H. T. Lee,[46] S. C. Lee,[47] H. L. Li,[23] J. Q. Li,[34] M. Li,[1] Q. Li,[34] Q. Y. Li,[23] S. Li,[1] S. L. Li,[6,7] J. H. Li,[22] Z. H. Li,[6,7] J. Liang,[22] M. J. Liang,[6,7] C. Light,[20] C. H. Lin,[47] T. Lippert,[24] J. H. Liu,[5] S. Q. Lu,[47] Y. S. Lu,[6] K. Luebelsmeyer,[1] J. Z. Luo,[34] Xi Luo,[23] F. Machate,[1] C. Mañá,[29] J. Marín,[29] J. Marquardt,[25] T. Martin,[10,21] G. Martínez,[29] N. Masi,[8,9] D. Maurin,[17] T. Medvedeva,[10] A. Menchaca-Rocha,[30] Q. Meng,[34] V. V. Mikhailov,[33] M. Molero,[29] P. Mott,[10,21] L. Mussolin,[36,37] J. Negrete,[20] N. Nikonov,[1] F. Nozzoli,[39] J. Ocampo-Peleteiro,[29] A. Oliva,[8] M. Orcinha,[27] M. Palermo,[20] F. Palmonari,[8,9] M. Paniccia,[16] A. Pashnin,[10] M. Pauluzzi,[36,37] S. Pensotti,[31,32] V. Plyaskin,[10] M. Pohl,[16] S. Poluianov,[35] X. Qin,[10] Z. Y. Qu,[47,23] L. Quadrani,[8,9] P. G. Rancoita,[31] D. Rapin,[16] A. Reina Conde,[26,8] E. Robyn,[16] S. Rosier-Lees,[3] A. Rozhkov,[10] D. Rozza,[31,32] R. Sagdeev,[11] S. Schael,[1] A. Schultz von Dratzig,[1] G. Schwering,[1] E. S. Seo,[12] B. S. Shan,[4] T. Siedenburg,[1] J. W. Song,[22] X. J. Song,[23] R. Sonnabend,[1] L. Strigari,[42,‡] T. Su,[23] Q. Sun,[22] Z. T. Sun,[6,7] M. Tacconi,[31,32] X. W. Tang,[6] Z. C. Tang,[6] J. Tian,[36,37] Samuel C. C. Ting,[10,15] S. M. Ting,[10] N. Tomassetti,[36,37] J. Torsti,[49] T. Urban,[10,21] I. Usoskin,[35] V. Vagelli,[41,36] R. Vainio,[49] M. Valencia-Otero,[48] E. Valente,[42,43] E. Valtonen,[49] M. Vázquez Acosta,[26] M. Vecchi,[18] M. Velasco,[29] J. P. Vialle,[3] C. X. Wang,[22] L. Wang,[5] L. Q. Wang,[22] N. H. Wang,[22] Q. L. Wang,[5] S. Wang,[20] X. Wang,[10] Yu Wang,[22] Z. M. Wang,[23] J. Wei,[16,23] Z. L. Weng,[10] H. Wu,[34] R. Q. Xiong,[34] W. Xu,[22,23] Q. Yan,[10] Y. Yang,[45] I. I. Yashin,[33] H. Yi,[34] Y. M. Yu,[10] Z. Q. Yu,[6] M. Zannoni,[31,32] C. Zhang,[6] F. Zhang,[6] F. Z. Zhang,[6,7] J. H. Zhang,[34] Z. Zhang,[10] F. Zhao,[6,7] C. Zheng,[23] Z. M. Zheng,[4] H. L. Zhuang,[6] V. Zhukov,[1] A. Zichichi,[8,9] and P. Zuccon[39,40]

(AMS Collaboration)

[1]*I. Physics Institute and JARA-FAME, RWTH Aachen University, 52056 Aachen, Germany*
[2]*Department of Physics, Middle East Technical University (METU), 06800 Ankara, Turkey*
[3]*Université Grenoble Alpes, Université Savoie Mont Blanc, CNRS, LAPP-IN2P3, 74000 Annecy, France*
[4]*Beihang University (BUAA), Beijing 100191, China*
[5]*Institute of Electrical Engineering (IEE), Chinese Academy of Sciences, Beijing 100190, China*
[6]*Institute of High Energy Physics (IHEP), Chinese Academy of Sciences, Beijing 100049, China*
[7]*University of Chinese Academy of Sciences (UCAS), Beijing 100049, China*
[8]*INFN Sezione di Bologna, 40126 Bologna, Italy*
[9]*Università di Bologna, 40126 Bologna, Italy*
[10]*Massachusetts Institute of Technology (MIT), Cambridge, Massachusetts 02139, USA*
[11]*East-West Center for Space Science, University of Maryland, College Park, Maryland 20742, USA*
[12]*IPST, University of Maryland, College Park, Maryland 20742, USA*
[13]*CHEP, Kyungpook National University, 41566 Daegu, Korea*
[14]*CNR-IROE, 50125 Firenze, Italy*
[15]*European Organization for Nuclear Research (CERN), 1211 Geneva 23, Switzerland*
[16]*DPNC, Université de Genève, 1211 Genève 4, Switzerland*
[17]*Université Grenoble Alpes, CNRS, Grenoble INP, LPSC-IN2P3, 38000 Grenoble, France*
[18]*Kapteyn Astronomical Institute, University of Groningen, P.O. Box 800, 9700 AV Groningen, Netherlands*
[19]*Sun Yat-Sen University (SYSU), Guangzhou 510275, China*
[20]*Physics and Astronomy Department, University of Hawaii, Honolulu, Hawaii 96822, USA*

[21]National Aeronautics and Space Administration Johnson Space Center (JSC), Houston, Texas 77058, USA
[22]Shandong University (SDU), Jinan, Shandong 250100, China
[23]Shandong Institute of Advanced Technology (SDIAT), Jinan, Shandong 250100, China
[24]Jülich Supercomputing Centre and JARA-FAME, Research Centre Jülich, 52425 Jülich, Germany
[25]Institut für Experimentelle und Angewandte Physik, Christian-Alberts-Universität zu Kiel, 24118 Kiel, Germany
[26]Instituto de Astrofísica de Canarias (IAC), 38205 La Laguna, and Departamento de Astrofísica, Universidad de La Laguna, 38206 La Laguna, Tenerife, Spain
[27]Laboratório de Instrumentação e Física Experimental de Partículas (LIP), 1649-003 Lisboa, Portugal
[28]National Chung-Shan Institute of Science and Technology (NCSIST), Longtan, Tao Yuan 32546, Taiwan
[29]Centro de Investigaciones Energéticas, Medioambientales y Tecnológicas (CIEMAT), 28040 Madrid, Spain
[30]Instituto de Física, Universidad Nacional Autónoma de México (UNAM), Ciudad de México 01000, Mexico
[31]INFN Sezione di Milano–Bicocca, 20126 Milano, Italy
[32]Università di Milano–Bicocca, 20126 Milano, Italy
[33]NRNU MEPhI (Moscow Engineering Physics Institute), Moscow 115409, Russia
[34]Southeast University (SEU), Nanjing 210096, China
[35]Sodankylä Geophysical Observatory and Space Physics and Astronomy Research Unit, University of Oulu, 90014 Oulu, Finland
[36]INFN Sezione di Perugia, 06100 Perugia, Italy
[37]Università di Perugia, 06100 Perugia, Italy
[38]INFN Sezione di Pisa, 56100 Pisa, Italy
[39]INFN TIFPA, 38123 Povo, Trento, Italy
[40]Università di Trento, 38123 Povo, Trento, Italy
[41]Agenzia Spaziale Italiana (ASI), 00133 Roma, Italy
[42]INFN Sezione di Roma 1, 00185 Roma, Italy
[43]Università di Roma La Sapienza, 00185 Roma, Italy
[44]INFN Sezione di Roma Tor Vergata, 00133 Roma, Italy
[45]National Cheng Kung University, Tainan 70101, Taiwan
[46]Academia Sinica Grid Center (ASGC), Nankang, Taipei 11529, Taiwan
[47]Institute of Physics, Academia Sinica, Nankang, Taipei 11529, Taiwan
[48]Physics Department and Center for High Energy and High Field Physics, National Central University (NCU), Tao Yuan 32054, Taiwan
[49]Space Research Laboratory, Department of Physics and Astronomy, University of Turku, 20014 Turku, Finland

(Received 1 March 2022; accepted 6 May 2022; published 10 June 2022)

We present the precision measurement of 2824 daily helium fluxes in cosmic rays from May 20, 2011 to October 29, 2019 in the rigidity interval from 1.71 to 100 GV based on 7.6×10^8 helium nuclei collected with the Alpha Magnetic Spectrometer (AMS) aboard the International Space Station. The helium flux and the helium to proton flux ratio exhibit variations on multiple timescales. In nearly all the time intervals from 2014 to 2018, we observed recurrent helium flux variations with a period of 27 days. Shorter periods of 9 days and 13.5 days are observed in 2016. The strength of all three periodicities changes with time and rigidity. In the entire time period, we found that below ∼7 GV the helium flux exhibits larger time variations than the proton flux, and above ∼7 GV the helium to proton flux ratio is time independent. Remarkably, below 2.4 GV a hysteresis between the helium to proton flux ratio and the helium flux was observed at greater than the 7σ level. This shows that at low rigidity the modulation of the helium to proton flux ratio is different before and after the solar maximum in 2014.

DOI: 10.1103/PhysRevLett.128.231102

The temporal evolution of the interplanetary space environment causes cosmic-ray intensity variations. This is particularly visible at rigidities below 100 GV. These variations correlate with solar activity at different timescales [1,2]. The most significant long-term variation is the 11-yr solar cycle [3,4]. Shorter-scale variations can be either recurrent or nonrecurrent. The nonrecurrent variations are mainly due to the interactions of cosmic rays with strong transient disturbances in the interplanetary magnetic field, such as shock waves generated by interplanetary coronal mass ejections, especially during solar maxima, that can last from days to weeks [5,6]. Recurrent variations with a period of 27 days, corresponding to the synodic solar rotation, and at multiples of that frequency (e.g., periods of 13.5 and 9 days) are related to the passage of corotating

interaction regions originating from one or more coronal holes of the Sun [7–15], as first observed in 1938 [16]. Neutron monitor studies on the estimated rigidity dependence in periodicities, for example, in Ref. [12], generally concluded that the power of the periodicity decreases with increasing rigidity. This formed the paradigm over the Alpha Magnetic Spectrometer (AMS) rigidity range (1.71–100 GV) that the strength of the 27-day (and 13.5- and 9-day) periodicities steadily decreases with increasing rigidity of cosmic rays, differently in solar maximum and minimum [17]. However, recent AMS results on periodicities in the proton daily fluxes [18] do not support that the strength of the periodicities would always decrease with increasing rigidity.

Cosmic-ray transport in the heliosphere is rigidity dependent. Hence, the time variation of different particle spectra (p, He, etc.) evaluated at the same rigidity are expected to exhibit a similar behavior. However, according to models based on the Parker equation [1], the time dependence of distinct nuclei fluxes evaluated at the same rigidity might differ because of (a) differences in the flux rigidity dependence outside the heliosphere, (b) differences in velocity because of distinct mass-to-charge ratio [19], and (c) solar wind turbulence and other interplanetary parameters.

Previously, AMS has reported the time dependence of proton and helium fluxes on the timescale of Bartels rotations (BR, 27 days). A significant long-term time dependence was observed in the p/He flux ratio at rigidities below 3 GV [20].

In the past, many experiments measured the time variation of proton and helium fluxes [21]. In this Letter, we present the daily time evolution of the helium flux from 1.71 to 100 GV. The measurement is based on 7.6×10^8 helium nuclei collected by AMS during the first 8.5 yr (May 20, 2011 to October 29, 2019, a total of 2824 days or 114 BRs) of operation aboard the International Space Station. For the first time, daily helium and proton fluxes are simultaneously measured from 1.71 to 100 GV. This is also the first continuous daily measurement of the rigidity dependence of 9-, 13.5-, and 27-day periodicities in the helium fluxes over an extended period of time and a broad range of rigidities.

Detector.—The layout and description of the AMS detector are presented in Refs. [22,23] and shown in Fig. S1 in Supplemental Material [24]. The key elements used in this measurement are the permanent magnet [25], the silicon tracker [26–28], and the four planes of time of flight scintillation counters [29]. Further information on the AMS layout, performance, trigger, and the Monte Carlo (MC) simulation [30,31] is detailed in Supplemental Material [24].

Event selection.—AMS has collected 1.5×10^{11} cosmic-ray events from May 20, 2011 to October 29, 2019. Helium events are required to be downward going and to have a reconstructed track in the inner tracker. See Fig. S2 in Supplemental Material [24] for a reconstructed helium event. Details of the event selection and backgrounds are contained in Refs. [20,32–36] and in Supplemental Material [24]. After selection, the event sample contains 7.6×10^8 helium nuclei.

Data analysis.—The daily isotropic flux Φ_i^j in the ith rigidity bin $(R_i, R_i + \Delta R_i)$ and jth day is given by

$$\Phi_i^j = \frac{N_i^j}{A_i^j \epsilon_i^j T_i^j \Delta R_i}, \tag{1}$$

where N_i^j is the number of events corrected for bin-to-bin migration, A_i^j is the effective acceptance, ϵ_i^j is the trigger efficiency, and T_i^j is the daily collection time. In this Letter, the helium flux was measured in 26 bins from 1.71 to 100 GV. Bin-to-bin migration of events was corrected using the unfolding procedures described in Ref. [37] independently for each day.

Extensive studies were made of the systematic errors [33]. These errors include the uncertainties in the background evaluation, the trigger efficiency, the geomagnetic cutoff, the acceptance calculation, the rigidity resolution function, the unfolding, and the absolute rigidity scale.

The time-dependent systematic error on the helium fluxes associated with the daily trigger efficiency measurement is $< 1\%$ over the entire rigidity range and for all days.

The geomagnetic cutoff was calculated as described in Supplemental Material [24], and the resulting systematic error on the fluxes is negligible ($< 0.4\%$) over the entire (1.71–100 GV) rigidity range.

The daily effective acceptances A_i^j were calculated using MC simulation and corrected for small differences between the data and simulated events related to (a) event reconstruction and selection, namely, in the efficiencies of velocity vector determination, track finding, charge determination, and tracker quality cuts, and (b) the details of inelastic interactions of nuclei in the AMS materials. The time-dependent systematic error on the fluxes associated with the daily reconstruction efficiencies is $< 1\%$ over the entire rigidity range for all days. The material traversed by nuclei within AMS is composed primarily of carbon and aluminum. The survival probabilities of helium due to interactions in the materials were measured using cosmic-ray data collected by AMS as described in Ref. [31]. Short-term variations, due to temperature changes, are small ($< 0.2\%$). Long-term variations ($< 3\%$), due to monitored minute changes in detector elements, are included in the MC simulation. After the time-dependent corrections, the daily effective acceptances and the daily reconstruction efficiencies are constant within errors. The time-independent systematic error on the helium fluxes due to uncertainties in the evaluation of the inelastic interactions is $< 1\%$ over the entire rigidity range [32].

The time-independent rigidity resolution function for helium has a pronounced Gaussian core and non-Gaussian tails. The systematic error on the fluxes due to the rigidity resolution function was obtained by repeating the unfolding procedure while independently varying the width of the Gaussian core by 5% and the amplitude of the non-Gaussian tails by 10% [33]. The resulting systematic error on the fluxes is $< 1\%$ in the entire rigidity range. The daily flux variation leads to an additional uncertainty in the unfolding procedure. The resulting time-dependent systematic error is $< 1.3\%$ at 1.71 GV and is negligible ($< 0.2\%$) above 5 GV for all days.

There are two contributions to the systematic uncertainty on the rigidity scale [37]. The first is due to residual tracker misalignment. This error was estimated by comparing the E/p ratio for electrons and positrons, where E is the energy measured with the electromagnetic calorimeter and p is the momentum measured with the tracker. It was found to be $1/30\ \mathrm{TV}^{-1}$ [38]. The error is negligible ($< 0.3\%$) below 100 GV. The second systematic error on the rigidity scale arises from the magnetic field map measurement and its temperature corrections. The total time-independent error on the fluxes due to uncertainty on the rigidity scale has been calculated to be $< 0.6\%$ over the rigidity range below 100 GV.

The contributions to the systematic error from the trigger efficiency, reconstruction efficiencies, and the unfolding are evaluated independently each day and are added in quadrature to derive a time-dependent systematic error, which is $< 1.5\%$ at 1.71 GV and $< 1\%$ above 3 GV for all days. The daily total systematic error is obtained by adding in quadrature the individual contributions of the time-independent systematic errors discussed above and the time-dependent systematic errors. At 1.71 GV it is $< 2.4\%$, and above 3 GV it is $< 1.4\%$ for all days.

Most importantly, several independent analyses were performed on the same data sample by different study groups. The results of those analyses are consistent with this Letter.

Results.—The measured daily helium fluxes (Φ_{He}) and helium to proton flux ratios ($\Phi_{\mathrm{He}}/\Phi_p$) including statistical errors, time-dependent systematic errors, and total systematic errors are tabulated in Tables S1–S2824 of Supplemental Material [24] as functions of the rigidity at the top of the AMS detector. The presented daily data are in agreement with our earlier 27-day results [20] in the overlapping time period, but with improved accuracy. The Φ_p data are from Ref. [18]. For the days when AMS detected solar energetic particles (SEPs), the fluxes below 3 GV will be included in a future publication [39] and not here.

Figure 1 shows Φ_{He} for six rigidity bins from 1.71 to 10.10 GV; see also Fig. S3 in Supplemental Material [24] for Φ_{He} in rectangular format. In this and subsequent figures, the error bars on the fluxes and flux ratios are

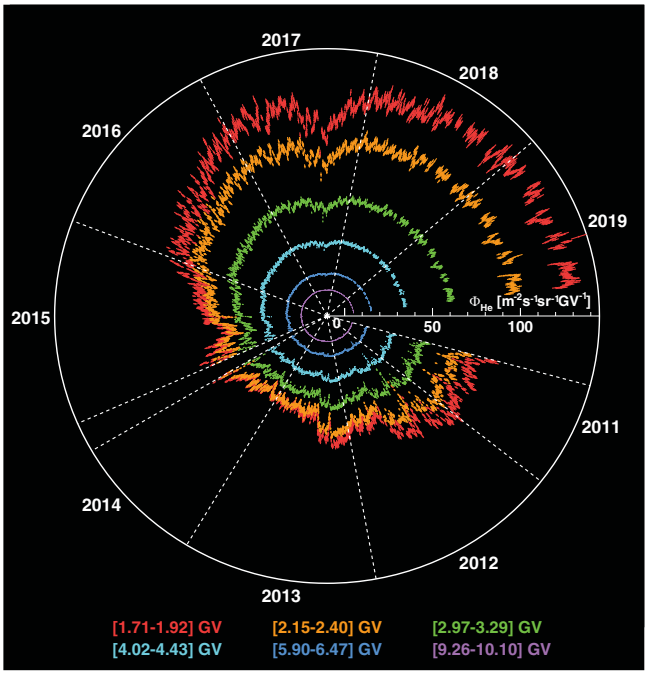

FIG. 1. The daily AMS helium fluxes Φ_{He} for six rigidity bins from 1.71 to 10.10 GV measured from May 20, 2011 to October 29, 2019 which includes a major portion of solar cycle 24 (from December 2008 to December 2019). The scale of daily helium fluxes Φ_{He} is shown on the radius. The AMS data cover the ascending phase, the maximum, and descending phase to the minimum of solar cycle 24. Days with SEPs are removed for the two lowest rigidity bins shown. The gaps in the fluxes are due to detector studies and upgrades. As seen, Φ_{He} exhibit large variations with time, and the relative magnitude of these variations decreases with increasing rigidity.

the sum in quadrature of the statistical and time-dependent systematic errors. As seen, the daily helium flux Φ_{He} exhibits variations on different timescales, from days to years (years are defined in Table SA in Supplemental Material [24]). The relative magnitude of these variations decreases with increasing rigidity. At low rigidities, recurrent flux variations are clearly visible. An explanation of the dip in 2017 is presented in Supplemental Material [24].

Figure S4 in Supplemental Material [24] shows Φ_{He} measured in 2016 for three rigidity bins [1.71–1.92], [5.90–6.47], and [16.60–22.80] GV. As seen, double-peak and triple-peak structures are visible in different Bartels rotations.

To study the recurrent time variations in Φ_{He}, a wavelet time-frequency technique [40] was used to locate the time intervals where the periodic structures emerge. The details on the wavelet analysis are described in Supplemental Material [24]. All the power spectra in the subsequent figures of the text and Supplemental Material [24] are drawn with normalized power defined in Supplemental Material [24] to show the strength of the periodicities. The Φ_{He} for three rigidity bins [1.71–1.92], [5.90–6.47], and

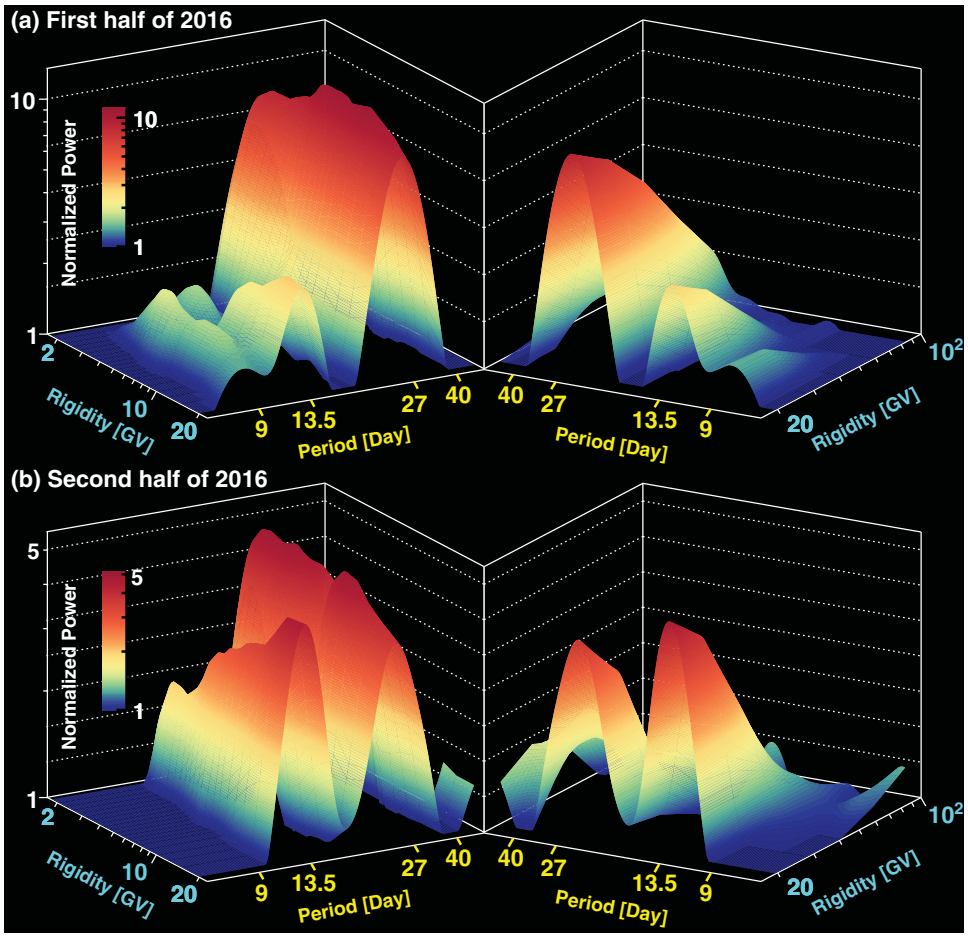

FIG. 2. The normalized power of helium fluxes as a function of rigidity and period for (a) the first and (b) the second half of 2016 from 1.71 to 20 GV and from 20 to 100 GV. As seen, the strength of 9-, 13.5-, and 27-day periodicities is rigidity dependent. In particular, the strength of 9-day periodicity in the first half of 2016 increases with increasing rigidity up to ~5 GV and then decreases with increasing rigidity up to 100 GV. The strength of 13.5-day periodicity in the second half of 2016 increases with increasing rigidity up to ~20 GV and then decreases with increasing rigidity up to 100 GV.

[16.60–22.80] GV in each of the nine years (2011–2019 defined in Table SA in Supplemental Material [24]), together with their time-averaged power spectra and 95% confidence levels, are shown in Figs. S5–S13 in Supplemental Material [24]. Similar to proton fluxes in Ref. [18], we observed recurrent flux variations with a period of ~27 days with a significance above the 95% confidence level in nearly all the time intervals from 2014 to 2018. Shorter periods of ~13.5 and ~9 days are significant only in 2016.

To study the details of periodicity in 2016, Fig. S14 in Supplemental Material [24] shows the wavelet time-frequency power spectra of Φ_{He} for the same three rigidity bins. As seen, periods of 9, 13.5, and 27 days are observed at different time intervals. The strength of all three periodicities changes with time and rigidity. In particular, shorter periods of 9 and 13.5 days, when present, are more visible at [5.90–6.47] and [16.60–22.80] GV compared to [1.71–1.92] GV. We define two time intervals of interest marked on the top of Fig. S14 in Supplemental Material [24]: The first time interval (BRs 2489–2495) is when the 9-day period is visible; the second time interval (BRs 2496–2502) is when the 9-day period is not visible.

Figure 2 shows the normalized power as a function of rigidity and period for the two time intervals (BRs 2489–2495 and 2496–2502); see also Fig. S15 in Supplemental Material [24] for details. The two figures show that the strength of all three periodicities is rigidity dependent. In particular, the strength of 9-day periodicity in the first half of 2016 increases with increasing rigidity up to ~5 GV. The strength of 13.5-day periodicity in the second half of 2016 increases with increasing rigidity up to ~20 GV. The strength of 27-day periodicity in the first half of 2016 increases with increasing rigidity up to ~10 GV. The AMS results on three periodicities (9-, 13.5-, and 27-day) from 1.71 to 100 GV show that the strength of the periodicities can increase with increasing rigidity and, thus, do not support the general conclusion that the strength of the

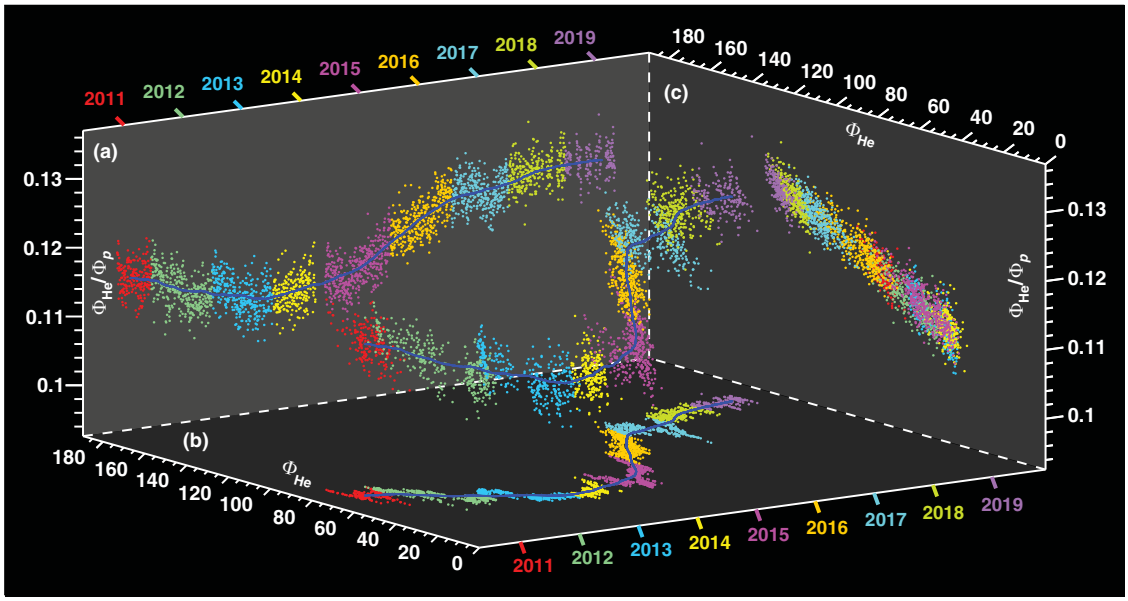

FIG. 3. The 3D functional dependence of (Φ_{He}/Φ_p, time, and Φ_{He} in units of $[m^2\,sr\,s\,GV]^{-1}$) for the rigidity bin [1.71–1.92] GV. (a) The dependence of Φ_{He}/Φ_p on time; (b) the dependence of Φ_{He} on time; (c) the relation between Φ_{He}/Φ_p and Φ_{He}. Different colors indicate different years from 2011 to 2019. The blue curves are moving averages of length 14 BRs with a step of one day.

periodicities of cosmic-ray fluxes decreases with increasing rigidity.

Note that both the unnormalized power of these periodicities and the flux variance in the two time intervals decrease with increasing rigidity as shown in Fig. S16 in Supplemental Material [24]. The peak values of the normalized power around 27 days as a function of rigidity for each year are shown in Fig. S17 in Supplemental Material [24]. As seen, the 27-day periodicity becomes significant only from 2014 to 2018, and its rigidity dependence varies in different time intervals.

The intensity variations of cosmic rays are caused by the temporal evolution of the interplanetary space environment [41] as discussed in Supplemental Material [24] and in Ref. [18] (see also Ref. [42]).

Figure 3 shows the 3D functional dependence of (Φ_{He}/Φ_p, time, and Φ_{He}) for the rigidity bin [1.71–1.92] GV. Moving averages of length 14 BRs with a step of one day are also shown. Figure 3(a) shows Φ_{He}/Φ_p as a function of time at this rigidity bin. As seen in Fig. 3(a) and Fig. S20 in Supplemental Material [24], Φ_{He}/Φ_p exhibits variations on multiple timescales. On short timescales, Φ_{He}/Φ_p has a dip in 2017 lasting months corresponding to the dip observed in Φ_{He} [Fig. 3(b)]. On long timescales, the Φ_{He}/Φ_p reaches a minimum in 2013–2014, when Φ_{He} is also in its minimum, and a maximum in 2018–2019, when Φ_{He} is also in its maximum. As shown in Fig. 3(a), $\Phi_{He}/\Phi_p(2018–2019) > \Phi_{He}/\Phi_p(2013–2014)$. This implies $\Phi_{He}(2018–2019)/\Phi_{He}(2013–2014) > \Phi_p(2018–2019)/\Phi_p(2013–2014)$; i.e., Φ_{He} exhibits larger time variations than Φ_p. Φ_{He}/Φ_p as a function of time for other rigidity bins is shown in Fig. S21 in Supplemental Material [24]. As seen, above ~7 GV, Φ_{He}/Φ_p is time independent. The comparison of $\Phi_{He}/\Phi_p(2018–2019)$ and $\Phi_{He}/\Phi_p(2013–2014)$ as a function of rigidity is shown in Fig. S22 in Supplemental Material [24]. As seen, Φ_{He} exhibits larger time variations than Φ_p below ~7 GV.

To investigate the difference of modulation in helium fluxes and proton fluxes, we consider in more detail daily Φ_{He}/Φ_p as a function of daily Φ_{He} as shown in Fig. 3(c). Figure 4 shows Φ_{He}/Φ_p as a function of Φ_{He} both calculated with the moving average of length 14 BRs with a step of one day for the rigidity bins [1.71–1.92] and [2.15–2.40] GV. As seen in Fig. 4, below 2.4 GV, a hysteresis between Φ_{He}/Φ_p and Φ_{He} is observed before and after the solar maximum in 2014. To assess the significance of this hysteresis, in Fig. S23 in Supplemental Material [24], we study the difference (in units of σ) of Φ_{He}/Φ_p at the same Φ_{He} but different solar conditions. As seen, the hysteresis is observed at ~6σ in each of the three consecutive rigidity bins below 2.4 GV, with a combined significance greater than 7σ. The same investigation is performed on daily Φ_{He}/Φ_p as a function of daily Φ_p as shown in Figs. S24–S26 in Supplemental Material [24]. As seen in Fig. S26 in Supplemental Material [24], the hysteresis between Φ_{He}/Φ_p and Φ_p is observed at greater than 6σ in each of the three consecutive rigidity bins below 2.4 GV, with a combined significance greater than 7σ. These combined significances show that at low rigidity the modulation of Φ_{He}/Φ_p is different before and after the solar maximum in 2014. These unexpected observations provide inputs to the understanding of cosmic-ray

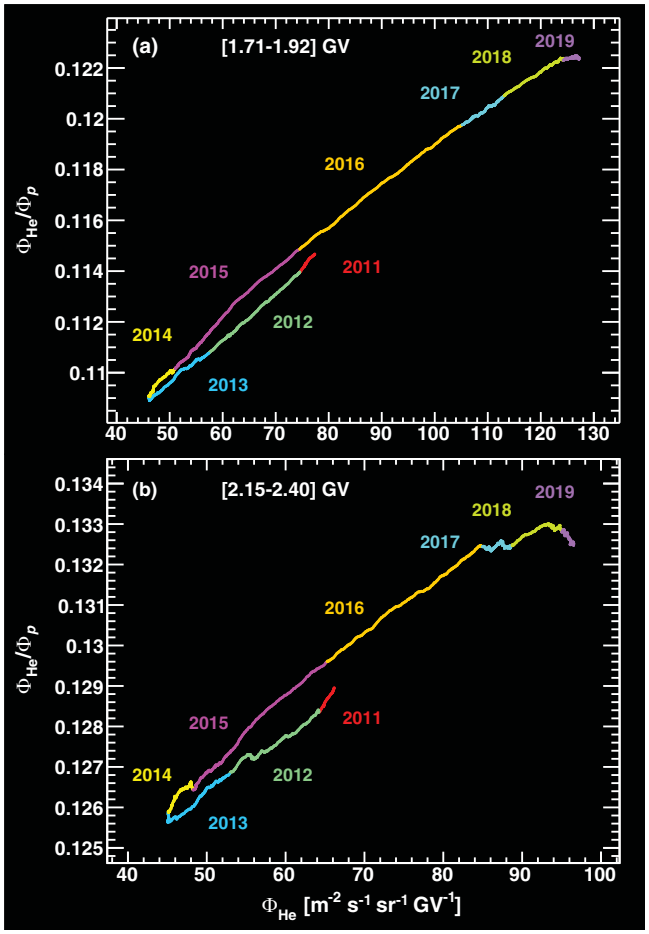

FIG. 4. $\Phi_{\mathrm{He}}/\Phi_p$ as a function of Φ_{He} both calculated with a moving average of length 14 BRs with a step of one day for the rigidity bins (a) [1.71–1.92] and (b) [2.15–2.40] GV. Different colors indicate different years from 2011 to 2019. As seen, below 2.4 GV a hysteresis between $\Phi_{\mathrm{He}}/\Phi_p$ and Φ_{He} is observed before and after the solar maximum in 2014.

propagation in the heliosphere and its dependence on rigidity, on velocity, on solar wind turbulence, and on other interplanetary parameters.

In conclusion, we have presented the precision measurements of 2824 daily helium fluxes in cosmic rays from 1.71 to 100 GV between May 20, 2011 and October 29, 2019 based on 7.6×10^8 helium nuclei. The helium flux Φ_{He} and the helium to proton flux ratio $\Phi_{\mathrm{He}}/\Phi_p$ exhibit variations on multiple timescales. In nearly all the time intervals from 2014 to 2018, we observed recurrent flux variations with a period of 27 days. Shorter periods of 9 and 13.5 days are observed in 2016. The strength of all three periodicities changes with both time and rigidity. In the entire time period, we found that below ~7 GV the helium flux exhibits larger time variations than the proton flux, and above ~7 GV the helium to proton flux ratio is time independent. Remarkably, below 2.4 GV, a hysteresis between the helium to proton flux ratio and the helium flux was observed at greater than the 7σ level. This shows that at low rigidity the modulation of the helium to proton flux ratio is different before and after the solar maximum in 2014. These results provide unique inputs to the understanding of cosmic rays in the heliosphere.

We are grateful for important physics discussions with Igor Moskalenko. We thank former NASA Administrator Daniel S. Goldin for his dedication to the legacy of the International Space Station (ISS) as a scientific laboratory and his decision for NASA to fly AMS as a DOE payload. We also acknowledge the continuous support of the NASA leadership, particularly William H. Gerstenmaier, and of the JSC and MSFC flight control teams that have allowed AMS to operate optimally on the ISS for over ten years. We are grateful for the support of Jim Siegrist, Glen Crawford, and their staff of the DOE including resources from the National Energy Research Scientific Computing Center under Contract No. DE-AC02-05CH11231. We acknowledge the strong support from Fabiola Gianotti, DG of CERN, and the CERN IT department including Bernd Panzer-Steindel. We also acknowledge the continuous support from MIT and its School of Science, and the Laboratory for Nuclear Science, Boleslaw Wyslouch. Research supported by Chinese Academy of Sciences, Institute of High Energy Physics, Institute of Electrical Engineering, China Academy of Space Technology, National Natural Science Foundation, and Ministry of Science and Technology, the China Scholarship Council, the provincial governments of Shandong, Jiangsu, Guangdong, Shandong University, and the Shandong Institute of Advanced Technology, China; CNRS/IN2P3 and CNES, France; DLR under Grant No. 50OO1805 and computing support on the JARA Partition of the RWTH Aachen supercomputer, and DLR under Grant No. 50OC1804 at CAU, Germany; INFN and ASI under ASI-INFN Agreements No. 2014-037-R.1-2017 and No. 2019-19-HH.0 and ASI-University of Perugia Agreement No. 2019-2-HH.0, Italy; CHEP and NRF under Grant No. NRF-2018R1A6A1A06024970 at Kyungpook National University, Korea; the Consejo Nacional de Ciencia y Tecnología and UNAM, Mexico; NWO under Grant No. 680-1-004, Netherlands; FCT under Grant No. CERN/FIS-PAR/0013/2019, Portugal; the Ministry of Science and Higher Education under Project No. 0723-2020-0040, Russia; CIEMAT, IAC, CDTI, and SEIDI-MINECO under Grants No. PID2019–107988 GB-C21/C22, No. CEX2019-000920-S, and No. MDM-2015-0509, Spain; federal and cantonal authorities and the Fondation Dr. Manfred Steuer, Switzerland; Academia Sinica and the Ministry of Science and Technology (MOST) under Grants No. 107-2119-M-006-015-MY3, No. 109-2112-M-001-029, and No. CDA-105-M06, former Presidents of Academia Sinica Yuan-Tseh Lee and Chi-Huey Wong and former Ministers of MOST Maw-Kuen Wu and Luo-Chuan Lee, Taiwan; the Turkish Energy, Nuclear and Mineral Research Agency (TENMAK) under

Grants No. 2020TAEK(CERN)A5.H1.F5-26, Turkey; and NSF Grants No. 1455202 and No. 2013228, Wyle Laboratories Grant No. 2014/T72497, and NASA NESSF Grant No. HELIO15F-0005, USA.

*Also at Nikhef, 1098 XG Amsterdam, Netherlands.
†Also at ASI Space Science Data Center (SSDC), 00133 Roma, Italy.
‡Also at Policlinico S. Orsola-Malpighi, 40138 Bologna, Italy.

[1] E. N. Parker, The passage of energetic charged particles through interplanetary space, Planet. Space Sci. **13**, 9 (1965).
[2] M. S. Potgieter, Solar modulation of cosmic rays, Living Rev. Solar Phys. **10**, 3 (2013).
[3] D. H. Hathaway, The solar cycle, Living Rev. Solar Phys. **12**, 4 (2015).
[4] Sunspot data from the World Data Center SILSO, Royal Observatory of Belgium, Brussels at http://www.sidc.be/silso/cyclesminmax.
[5] M. Zhang, Modulation of galactic cosmic rays at solar maximum: Observations, Adv. Space Res. **32**, 603 (2003); H. V. Cane, Coronal mass ejections and Forbush decreases, Space Sci. Rev. **93**, 55 (2000); M. S. Potgieter, J. A. Le Roux, L. F. Burlaga, and F. B. McDonald, The role of merged interaction regions and drifts in the heliospheric modulation of cosmic rays beyond 20 AU: A computer simulation, Astrophys. J. **403**, 760 (1993); G. Wibberenz, I. G. Richardson, and H. V. Cane, A simple concept for modeling cosmic ray modulation in the inner heliosphere during solar cycles 20-23, J. Geophys. Res. **107**, 1353 (2002).
[6] R. Munini *et al.*, Evidence of energy and charge sign dependence of the recovery time for the 2006 December Forbush event measured by the PAMELA experiment, Astrophys. J. **853**, 76 (2018).
[7] J. A. Simpson, A brief history of recurrent solar modulation of the galactic cosmic rays (1937-1990), Space Sci. Rev. **83**, 169 (1998).
[8] C. Paizis, B. Heber, P. Ferrando, A. Raviart, B. Falconi, S. Marzolla, M. S. Potgieter, V. Bothmer, H. Kunow, R. Müller-Mellin, and A. Posner, Amplitude evolution and rigidity dependence of the 26-day recurrent cosmic ray decreases: COSPIN/KET results, J. Geophys. Res. **104**, 28241 (1999).
[9] Z. Shen, G. Qin, P. Zuo, F. Wei, and X. Xu, A study of variations of galactic cosmic-ray intensity based on a hybrid data-processing method, Astrophys. J. **900**, 143 (2020).
[10] R. Modzelewska *et al.*, Study of the 27 day variations in GCR fluxes during 2007-2008 based on PAMELA and ARINA observations, Astrophys. J. **904**, 3 (2020). In this paper, the rigidity dependence of the 27-day periodicity in 2007–2008 has been directly measured.
[11] R. Modzelewska and A. Gil, Recurrence of galactic cosmic-ray intensity and anisotropy in solar minima 23/24 and 24/25 observed by ACE/CRIS, STEREO, SOHO/EPHIN and neutron monitors, Astron. Astrophys. **646**, A128 (2021).
[12] A. López-Comazzi and J. J. Blanco, Short-term periodicities observed in neutron monitor counting rates, Sol. Phys. **295**, 81 (2020).
[13] M. Armano *et al.*, Characteristics and energy dependence of recurrent galactic cosmic-ray flux depressions and of a Forbush decrease with LISA pathfinder, Astrophys. J. **854**, 113 (2018).
[14] I. Sabbah and K. Kudela, Third harmonic of the 27 day periodicity of galactic cosmic rays: Coupling with interplanetary parameters, J. Geophys. Res. **116**, n/a (2011).
[15] M. Temmer, B. Vršnak, and A. M. Veronig, Periodic appearance of coronal holes and the related variation of solar wind parameters, Sol. Phys. **241**, 371 (2007).
[16] S. E. Forbush, On cosmic ray effects associated with magnetic storms, Terr. Magn. Atmos. Electr. **43**, 203 (1938).
[17] A. Gil and M. V. Alania, Theoretical and experimental studies of the rigidity spectrum of the 27-day variation of the galactic cosmic ray intensity in different epochs of solar activity, Sol. Phys. **283**, 565 (2013).
[18] M. Aguilar *et al.*, Periodicities in the Daily Proton Fluxes from 2011 to 2019 Measured by the Alpha Magnetic Spectrometer on the International Space Station from 1 to 100 GV, Phys. Rev. Lett. **127**, 271102 (2021).
[19] C. Corti, M. S. Potgieter, V. Bindi, C. Consolandi, C. Light, M. Palermo, and A. Popkow, Numerical modeling of galactic cosmic-ray proton and helium observed by AMS-02 during the solar maximum of Solar Cycle 24, Astrophys. J. **871**, 253 (2019); N. Tomassetti, F. Barão, B. Bertucci, E. Fiandrini, and M. Orcinha, Numerical modeling of cosmic-ray transport in the heliosphere and interpretation of the proton-to-helium ratio in Solar Cycle 24, Adv. Space Res. **64**, 2477 (2019); M. D. Ngobeni, O. P. M. Aslam, D. Bisschoff, M. S. Potgieter, D. C. Ndiitwani, M. Boezio, N. Marcelli, R. Munini, V. V. Mikhailov, and S. A. Koldobskiy, The 3D numerical modeling of the solar modulation of galactic protons and helium nuclei related to observations by PAMELA between 2006 and 2009, Astrophys. Space Sci. **365**, 182 (2020).
[20] M. Aguilar *et al.*, Observation of Fine Time Structures in the Cosmic Proton and Helium Fluxes with the Alpha Magnetic Spectrometer on the International Space Station, Phys. Rev. Lett. **121**, 051101 (2018).
[21] V. K. Balasubrahmanyan, E. Boldt, and R. A. R. Palmeira, Low-energy spectrum of cosmic rays as an indicator of primary source characteristics and interstellar propagation, Phys. Rev. **140**, B1157 (1965); Solar modulation of galactic cosmic rays, J. Geophys. Res. **72**, 27 (1967); J. F. Ormes and W. R. Webber, Proton and helium nuclei cosmic-ray spectra and modulations between 100 and 2000 Mev/nucleon, J. Geophys. Res. **73**, 4231 (1968); J. A. Lezniak and W. R. Webber, Solar modulation of cosmic ray protons, helium nuclei, and electrons: A comparison of experiment with theory, J. Geophys. Res. **76**, 1605 (1971); D. E. Stilwell, R. M. Joyce, B. J. Teegarden, J. H. Trainor, G. Streeter, and J. Bernstein, The Pioneer 10/11 and Helios A/B cosmic ray instruments, IEEE Trans. Nucl. Sci. **22**, 570 (1975); G. M. Mason and W. W. Mixon, The University of Chicago Charged Particle Experiments on IMP-7 and IMP-8 Instrument and Data Format Specifications, NSSDC Technical

Report File Number B23906-000A, 1975; E. T. Sarris, S. M. Krimigis, and T. P. Armstrong, Observations of magnetospheric bursts of high-energy protons and electrons at ~35 R_E with Imp 7, J. Geophys. Res. **81**, 2341 (1976); R. E. McGuire, T. T. von Rosenvinge, and F. B. McDonald, The composition of solar energetic particles, Astrophys. J. **301**, 938 (1986); E. C. Stone *et al.*, Cosmic ray investigation for the Voyager missions; energetic particle studies in the outer heliosphere-And beyond, Space Sci. Rev. **21**, 355 (1977); J. A. Simpson *et al.*, The ULYSSES cosmic ray and solar particle investigation, Astron. Astrophys. Suppl. Ser. **92**, 365 (1992); J. Torsti *et al.*, Energetic particle experiment ERNE, Sol. Phys. **162**, 505 (1995); E. C. Stone, A. M. Frandsen, R. A. Mewaldt, E. R. Christian, D. Margolies, J. F. Ormes, and F. Snow, The advanced composition explorer, Space Sci. Rev. **86**, 1 (1998); Y. Shikaze *et al.*, Measurements of 0.2–20 GeV/n cosmic-ray proton and helium spectra from 1997 through 2002 with the BESS spectrometer, Astropart. Phys. **28**, 154 (2007); T. T. von Rosenvinge *et al.*, The high energy telescope for STEREO, Space Sci. Rev. **136**, 391 (2008); D. J. McComas *et al.*, Integrated Science Investigation of the Sun (ISIS): Design of the energetic particle investigation, Space Sci. Rev. **204**, 187 (2016); K. Abe *et al.*, Measurements of cosmic-ray proton and helium spectra from the BESS-Polar long-duration balloon flights over Antarctica, Astrophys. J. **822**, 65 (2016); J. Rodríguez-Pacheco *et al.*, The energetic particle detector: Energetic particle instrument suite for the Solar Orbiter mission, Astron. Astrophys. **642**, A7 (2020); N. Marcelli *et al.*, Time dependence of the flux of helium nuclei in cosmic rays measured by the PAMELA experiment between 2006 July and 2009 December, Astrophys. J. **893**, 145 (2020); N. Marcelli *et al.*, Helium fluxes measured by the PAMELA experiment from the minimum to the maximum solar activity for Solar Cycle 24, Astrophys. J. **925**, L24 (2022).

[22] M. Aguilar *et al.*, The Alpha Magnetic Spectrometer (AMS) on the International Space Station: Part II—Results from the first seven years, Phys. Rep. **894**, 1 (2021).

[23] A. Kounine, The Alpha Magnetic Spectrometer on the International Space Station, Int. J. Mod. Phys. E **21**, 1230005 (2012); S. Rosier-Lees, New results from AMS, in *Proceedings of Astroparticle Physics TEVPA/IDM, Amsterdam*, 2014 (to be published); S. Ting, The Alpha Magnetic Spectrometer on the International Space Station, Nucl. Phys. B, Proc. Suppl. **243–244**, 12 (2013); S.-C. Lee, Latest Results from AMS, in *Proceedings of the 20th International Conference on Supersymmetry and Unification of Fundamental Interactions (SUSY 2012), Beijing*, 2012 (to be published); M. Aguilar, The AMS Experiment on the ISS, in *Proceedings of the XL International Meeting on Fundamental Physics, Centro de Ciencias de Benasque Pedro Pascual*, 2012 (to be published); S. Schael, Status of the AMS-02 experiment on the ISS, in *Proceedings of the 10th Symposium on Sources and Detection of Dark Matter and Dark Energy in the Universe, Los Angeles*, 2012 (to be published); B. Bertucci, The AMS-02 detector operation in space, *Proc. Sci.*, EPS-HEP (2011) 67; M. Incagli, Astroparticle Physiscs with AMS02, AIP Conf. Proc. **1223**, 43 (2010); R. Battiston, The antimatter spectrometer (AMS-02): A particle physics detector in space, Nucl. Instrum. Methods Phys. Res., Sect. A **588**, 227 (2008).

[24] See Supplemental Material at http://link.aps.org/supplemental/10.1103/PhysRevLett.128.231102 for the AMS detector description, details of event selection, definition of years, explanation of the dip in 2017, details of wavelet analysis, cross wavelet transformation of the properties of the interplanetary space environment, hysteresis analysis, figures, and the tabulated daily helium fluxes and He/p flux ratios as functions of rigidity. Note that the data can also be downloaded in different formats from the AMS Web site https://ams02.space/sites/default/files/publication/202201/table-s1-s2824.csv, the ASI cosmic-ray database at https://tools.ssdc.asi.it/CosmicRays, and the LPSC cosmic-day database at https://lpsc.in2p3.fr/crdb/.

[25] K. Lübelsmeyer *et al.*, Upgrade of the Alpha Magnetic Spectrometer (AMS-02) for long term operation on the International Space Station (ISS), Nucl. Instrum. Methods Phys. Res., Sect. A **654**, 639 (2011).

[26] B. Alpat *et al.*, The internal alignment and position resolution of the AMS-02 silicon tracker determined with cosmic-ray muons, Nucl. Instrum. Methods Phys. Res., Sect. A **613**, 207 (2010).

[27] G. Ambrosi, V. Choutko, C. Delgado, A. Oliva, Q. Yan, and Y. Li, The spatial resolution of the silicon tracker of the Alpha Magnetic Spectrometer, Nucl. Instrum. Methods Phys. Res., Sect. A **869**, 29 (2017).

[28] Y. Jia, Q. Yan, V. Choutko, H. Liu, and A. Oliva, Nuclei charge measurement by the Alpha Magnetic Spectrometer silicon tracker, Nucl. Instrum. Methods Phys. Res., Sect. A **972**, 164169 (2020).

[29] V. Bindi *et al.*, Calibration and performance of the AMS-02 time of flight detector in space, Nucl. Instrum. Methods Phys. Res., Sect. A **743**, 22 (2014).

[30] J. Allison *et al.*, Recent developments in GEANT4, Nucl. Instrum. Methods Phys. Res., Sect. A **835**, 186 (2016); GEANT4 developments and applications, IEEE Trans. Nucl. Sci. **53**, 270 (2006); S. Agostinelli *et al.*, GEANT4-a simulation toolkit, Nucl. Instrum. Methods Phys. Res., Sect. A **506**, 250 (2003).

[31] Q. Yan, V. Choutko, A. Oliva, and M. Paniccia, Measurements of nuclear interaction cross sections with the Alpha Magnetic Spectrometer on the International Space Station, Nucl. Phys. **A996**, 121712 (2020).

[32] M. Aguilar *et al.*, Precision Measurement of the Helium Flux in Primary Cosmic Rays of Rigidities 1.9 GV to 3 TV with the Alpha Magnetic Spectrometer on the International Space Station, Phys. Rev. Lett. **115**, 211101 (2015).

[33] M. Aguilar *et al.*, Observation of the Identical Rigidity Dependence of He, C, and O Cosmic Rays at High Rigidities by the Alpha Magnetic Spectrometer on the International Space Station, Phys. Rev. Lett. **119**, 251101 (2017).

[34] M. Aguilar *et al.* (AMS Collaboration), Measurement of the Geomagnetic Cutoff with the Alpha Magnetic Spectrometer on the International Space Station (to be published).

[35] C. C. Finlay *et al.*, International geomagnetic reference field: The eleventh generation, Geophys. J. Int. **183**, 1216 (2010); E. Thébault *et al.*, International Geomagnetic Reference Field: The 12th generation, Earth Planets Space

67, 79 (2015); Geomagnetic Field Modeling Working Group, IGRF-13 model (2019), https://www.ngdc.noaa.gov/IAGA/vmod/igrf.html.

[36] P. Bobik, G. Boella, M. J. Boschini, D. Grandi, M. Gervasi, K. Kudela, S. Pensotti, and P. G. Rancoita, Magnetospheric transmission function approach to disentangle primary from secondary cosmic ray fluxes in the penumbra region, J. Geophys. Res. **111**, A05205 (2006); N. A. Tsyganenko and M. I. Sitnov, Modeling the dynamics of the inner magnetosphere during strong geomagnetic storms, J. Geophys. Res. **110**, A03208 (2005).

[37] M. Aguilar *et al.*, Precision Measurement of the Proton Flux in Primary Cosmic Rays from Rigidity 1 GV to 1.8 TV with the Alpha Magnetic Spectrometer on the International Space Station, Phys. Rev. Lett. **114**, 171103 (2015).

[38] J. Berdugo, V. Choutko, C. Delgado, and Q. Yan, Determination of the rigidity scale of the Alpha Magnetic Spectrometer, Nucl. Instrum. Methods Phys. Res., Sect. A **869**, 10 (2017).

[39] M. Aguilar *et al.* (AMS Collaboration), Measurement of the solar energetic particles with the alpha magnetic spectrometer on the International Space Station (to be published).

[40] C. Torrence and G. P. Compo, A practical guide to wavelet analysis, Bull. Am. Meteorol. Soc. **79**, 61 (1998).

[41] NASA/GSFC's OMNI data set at daily resolution: https://omniweb.gsfc.nasa.gov/.

[42] A. Grinsted, J. C. Moore, and S. Jevrejeva, Application of the cross wavelet transform and wavelet coherence to geophysical time series, Nonlinear Processes Geophys. **11**, 561 (2004).